

Article

Rapid Hydrolysis of Organophosphates Induced by U(IV) Nanoparticles: A Kinetic and Mechanistic Study using Spectroscopic Analysis

Hyejin Cho  and Wansik Cha * 

Nuclear Chemistry Research Division, Korea Atomic Energy Research Institute, Daedeok-daero, Yuseong-gu, Daejeon 989-111, Korea; hcho921@kaeri.re.kr

* Correspondence: wscha@kaeri.re.kr

Received: 8 September 2019; Accepted: 20 November 2019; Published: 26 November 2019



Abstract: The heterogeneous interactions of colloidal U particles with organophosphates, leading to the formation of U-phosphate minerals, can retard the migration of U in contaminated sites. Here, we studied the hydrolytic mechanism of *p*-nitrophenyl phosphate (NPP) on the surfaces of tetravalent uranium nanoparticles (U(IV)_{NPs}), resulting in the formation of U-phosphate precipitates. Our study shows that the reaction rate of NPP hydrolysis is significantly enhanced by U(IV)_{NPs} through a multi-step heterogeneous reaction on the particle surfaces. The end products of the reaction were identified as U(IV)_{NPs}-aggregates with surface-bound phosphates. Colloidal properties, such as high positive values of the zeta-potential (>+30 mV) and large surface areas of U(IV)_{NPs} due to their unique cluster structures consisting of relatively small primary UO₂(cr)-particles, are correlated with their reactivity towards hydrolysis reaction. Reaction kinetic modeling studies using spectrophotometric data indicated the presence of two distinct reaction intermediates as the surface complexes of NPP on U(IV)_{NPs}. We suggest the involvement of the NPP inner-sphere complexes in the rate-determining step based on the results obtained by analyzing the ATR-FTIR spectra and the surface-enhanced infrared absorption of NPP bound to substrate surfaces.

Keywords: tetravalent uranium nanoparticles (U(IV)_{NPs}); organophosphates; *p*-nitrophenyl phosphate (NPP); hydrolysis; surface complexation; surface-enhanced infrared absorption; heterogeneous reaction mechanism

1. Introduction

Tetravalent uranium(U(IV)) is generally considered an immobile species under reducing repository conditions due to its low solubility and strong tendency to be retained at mineral surfaces [1]. It is recognized, however, that U(IV) in aqueous solution is dominated by colloidal species under reducing conditions [2]. The generation of such colloids/nanoparticles can increase the amount of U in groundwater, and is higher than expected from their thermodynamic solubility; consequently, enhancing the possibility of their migration [3]. Further, U's colloidal behaviors can be influenced by various interactions, such as adsorption, complexation, and surface reaction on colloidal particles, with mineral compounds and organic materials in environments [4,5]. Thus, a precise understanding of the colloid-facilitated transport of U is required to establish the immobilization strategy of such colloids in U-contaminated sites.

Phosphates have been shown to immobilize U by sorption [6,7] and by facilitating the precipitation of U-bearing phosphate minerals [8,9]. These strategies utilize the poor mobility of phosphate within sediments by adsorption onto mineral phases, co-precipitation with metals and radionuclides, and ion-exchange reactions [10]. Murray et al. observed that U can be strongly adsorbed on apatite,

which has a high capacity for retaining U by phosphate mineralization [7]. Biotic approaches for immobilizing subsurface U were also examined using microbial phosphatase activities that promote the in situ sequestration of U as an insoluble phosphate mineral [11,12]. In the presence of organophosphates under reducing conditions, the biomineralization of U(VI)-phosphate minerals has been shown to be more effective for removing U than bioreduction to U(IV) species; e.g., uraninite. This is because biogenic U(IV) is considered to be prone to oxidative remobilization after exposure to oxygen or nitrate [13]. Furthermore, the ningyoite-like U(IV)-phosphate precipitates obtained by stimulating microbial U(VI) reduction in supplement with organophosphate (e.g., glycerol phosphate) exhibit high resistance to oxidative remobilization [12]. Also, mononuclear U(IV)-phosphate complexes and nanocrystalline U(IV) minerals were identified as major forms of U in laboratory bioreduction settings as well as in lake sediments possessing rich organic matter [14,15]. However, the chemical mechanism of U-phosphate mineralization as well as the reactivities of each U(IV/VI) species involved has not been separately evaluated so far.

In fact, the occurrence of phosphate via the decomposition of organophosphates and its adsorption to mineral phases have been extensively studied to understand the fate and cycle of the phosphorous present in natural waters, sediments, and soils [16–21]. It has been shown that various insoluble minerals in aqueous media, including anatase (TiO_2), goethite ($\alpha\text{-FeOOH}$), and MnO_2 , cause an increase in the rate of the hydrolysis of organophosphates [22–25]. Conversely, among the homogeneous catalytic systems in previous studies [26–31], highly charged metal cations, including lanthanides (Ln)(III), Ce(IV), and Th(IV), were found to be the most active complexes for the hydrolysis of phosphoesters [32–35]. These studies indicated that the Lewis acidities of these metals and the presence of bound hydroxide are crucial for stabilizing the transition state of phosphoester hydrolysis. However, due to the exceptionally low solubility of transition metal ions in aquatic environments, heterogeneous reactions involving suspended mineral phases, instead of homogeneous ones, may be crucial in the cycling of phosphorous.

To date, only few results regarding the interaction of U(IV) species with phosphate and organophosphates, which may accelerate or retard the migration of U, have been reported. In this study, we investigated the intrinsic reactivities of U(IV) toward the hydrolysis of phosphoesters using synthetic U(IV) species; i.e., a model U(IV) nanocolloidal system consisting of crystalline UO_2 phases at various reaction conditions. Spectrophotometry-based hydrolysis kinetic analysis and reaction modeling analysis were employed to understand the detailed reaction mechanism of the surface-promoted hydrolysis of phosphoesters on the U(IV) nanoparticles. In particular, we exploited the surface-enhanced infrared absorption phenomena of a model phosphoester on U(IV) nanoparticles for the first time to examine the heterogeneous reaction mechanism and the molecular structures of the surface complexes.

2. Materials and Methods

All chemicals, including *p*-nitrophenyl phosphate disodium salt hexahydrate (NPP) and *p*-nitrophenol (NPH) (reagent grade, Sigma-Aldrich), were used as purchased. All procedures for the sample preparation were conducted in an Ar-filled glove box.

2.1. Synthesis and Identification of U(IV) Species

2.1.1. U(IV) Nanoparticles ($\text{U(IV)}_{\text{NPs}}$)

The nanoparticle formation of U(IV) was induced in mild acidic aqueous solutions (pH 2–3). An aliquot of U(IV) stock solution (about 70 mM), which was electrochemically prepared in advance as described elsewhere [36], was added to a 0.1 M NaClO_4 solution in a 25 mL vial to prepare a 3 mM U(IV) solution. After 5 h of hydrothermal reaction at 90 °C, the solution's color changed from clear light blue to dark yellow. The $\text{U(IV)}_{\text{NPs}}$ we synthesized were stored in an Ar-filled glove box for subsequent use. High-resolution transmission electron microscopy (HR-TEM, JEOL, JEM 2001F) was applied to

determine particle size, morphology, and crystalline structure. Furthermore, dynamic light scattering (DLS)-based particle size and zeta-potential of the nanoparticles were measured intermittently for up to 8 weeks to confirm their colloidal stability.

2.1.2. Amorphous U(IV)-Hydroxides (U(IV)-OH(am))

Due to the low solubility of U(IV), hydrolyzed forms of U(IV) can be rapidly prepared by adding an aliquot of the acidic U(IV) stock solution directly into neutral or basic aqueous solutions. Typically, amorphous solid U(IV)-OH is obtained as bluish cloudy precipitates; i.e., a macro-scale solid phase network, that is normally accumulated at the bottom of a vessel as a soft cloudy layer, at room temperature.

2.2. Particle Size and Zeta-Potential Measurements

For characterization of the colloidal properties of the U(IV)_{NPs}, size and zeta-potential measurements were performed by the DLS method. Typically, 1 mM of U(IV)_{NPs} was prepared and subjected to measurements using a commercial DLS instrument (Zetasizer NanoZS, Malvern Instruments, Worcestershire, UK). The measurements were made at 25 °C in aqueous solutions containing 0.1 M NaClO₄, which is the typical electrolyte level of the NPP hydrolysis reaction media in this study. The solution's pH, ranging from 2 to 9, was adjusted using 0.1 M NaOH. Moreover, following the manufacturer's suggestion (Malvern Instruments), we applied the Smoluchowski approximation to calculate the zeta-potential (see SI for the measurement parameters). The data were collected and averaged from the zeta-potential average values of three runs. For the amorphous solid U(IV)-OH, its size distribution was too large to measure by DLS analysis.

2.3. Spectrophotometric Reaction Kinetic Analysis

The rates of the hydrolysis of NPP by U(IV) species were measured spectrophotometrically by monitoring the increase in the absorbance at 400 nm, which is the λ_{\max} of the reaction product, *p*-nitrophenolate (NP). A spectrophotometer (MCS601, Carl Zeiss, Jena, Germany) equipped with a temperature-controlled cell holder (Qpod 2e, Quantum Northwest, USA) was used for the measurements. Typically, aqueous solutions of 0.5 mM NPP and 3 mM U(IV) species were prepared in 0.1 M NaClO₄ and used for the sample preparation. A total of 300 μ L of 0.5 mM NPP was added to 2.7 mL of 0.1 M NaClO₄ solution in a quartz cuvette (cell path length of 1 cm). The pH was controlled by the addition of 0.1 M NaOH prior to the addition of the NPP. The reaction was typically initiated by the injection of 100 μ L of a 3 mM U(IV) solution (pH: 2.3) into the mixed solution when the temperature-controlled cell holder was set at the desired temperature (25 or 50 °C).

2.4. ATR-FTIR Measurements

Two sets of FTIR experiments for the NPP hydrolysis study were conducted using a spectrometer (Nicolet iS10™, Thermo Scientific) equipped with a single ATR module (GladiATR™, Pike Technologies) for solid samples and a 9-reflection diamond ATR module (LR-D-M, Durasens LLC) containing a liquid flow cell for liquid samples. Aqueous solutions of 0.15 mM NPP or phosphate with 1.5 mM U(IV)_{NPs} in 0.1 M NaClO₄ were stirred overnight at room temperature and subsequently centrifuged for 2 h with 132,380 RCF. The supernatant was removed and the remaining precipitate was washed with 0.01 M HCl to eliminate ClO₄⁻. The precipitate-HCl mixed solution was centrifuged for 0.5 h with 132,380 RCF. The supernatant was removed and the washed precipitates were freeze-dried for 3–4 h to obtain powder samples for the measurements. Alternatively, U(IV)_{NPs} for the other IR experiments were prepared in a chloride medium instead of perchlorate due to the presence of a strong perchlorate absorption band around 900–1100 cm⁻¹ in the spectra. Aqueous solution mixtures of NPP and U(IV)_{NPs} were prepared at various concentrations and pH levels, after which they were introduced within 10 min to the flow cell on the ATR-FTIR module for the measurements at room temperature.

2.5. Reaction Modeling Analysis

A reaction modeling study was conducted to confirm the measured reaction rate and the proposed reaction mechanism using the ReactLab KINETICS software (JPlus Consulting, East Fremantle, WA, Australia). The UV–Vis spectrophotometric data obtained from the reaction kinetic monitoring experiments were analyzed by the program. The global fitting of the reaction data was performed using a two-step reaction sequence.

3. Results and Discussion

3.1. Characterization of U(IV)_{NPs}

A hydrothermally induced U(IV)_{NPs} preparation method was developed using acidic U(IV) aqueous solutions (pH ~2). The acidity and concentration of U(IV), typically 3 mM in 0.1 M NaClO₄ solution, were controlled passively; i.e., by the dilution of an acidic U(IV) stock solution (pH < 1). We confirmed that the dominant U(IV) species before and after the synthesis were UOH³⁺(aq) and U(IV)_{NPs}, respectively (see Figure S1). The synthesis, storage, and tests of U(IV)_{NPs} were carried out under anaerobic conditions; e.g., in an Ar-filled glove box.

Figure 1a,b shows the transmission electron microscopy (TEM) images exhibiting a characteristic raspberry-type cluster morphology of U(IV)_{NPs} and crystalline-UO₂ internal structures of relatively small primary particles. The primary particles had a size distribution ranging from 3 to 6 nm based on the TEM image analysis. Interestingly, the presence of primary particles could not be detected by dynamic light scattering (DLS) analysis, the results of which display that U(IV)_{NPs} clusters were a major form of nanoparticles in aqueous solutions. The resulting U(IV)_{NPs} clusters were uniformly dispersed in the solution and exhibited rather monodisperse size distribution (see Figure S2), typically with the average cluster size of 23 ± 6 nm (uncertainty obtained from the results of several batches of U(IV)_{NPs}). Thus, in this article we use the term, U(IV)_{NPs}, to indicate the clusters of U(IV) primary particles, unless otherwise noted. We confirm that U(IV)_{NPs} are stable in an acidic solution (pH 1.5–2.4) over 8 weeks at room temperature, although in metastable colloidal states (see Figure 1c,d).

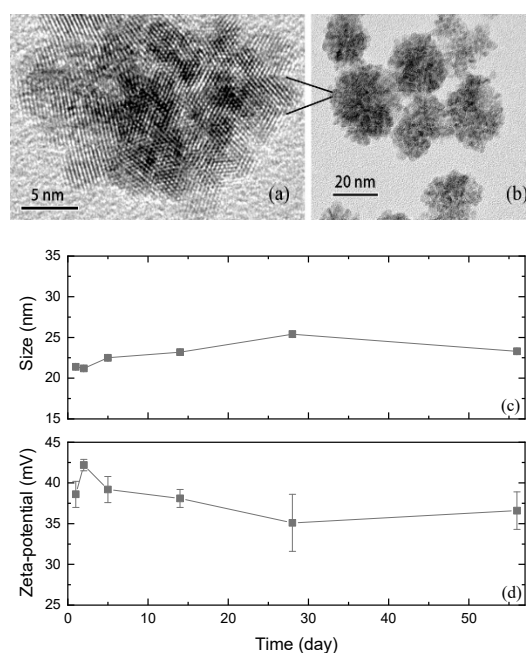


Figure 1. Characteristics of U(IV)_{NPs} synthesized in this study; TEM images showing (a) crystalline internal structures of primary particles and (b) their clusters of nominal particle sizes (20–30 nm); (c) particle size and (d) zeta-potential measurements of 1 mM U(IV)_{NPs} in 0.1 M NaClO₄ at pH 2.3 over time by DLS.

The acidic stock solutions of the synthesized $U(IV)_{NPs}$ display highly positive zeta-potential values in the range of +35 to +40 mV, providing a good explanation of the colloidal stabilities of these nanoparticles over the extended period (see Figure 1d). Thus, it is very likely that the inter-particle Coulombic repulsion resulting from the surface charges is a critical interfacial determinant of the colloidal stabilities of $U(IV)_{NPs}$ and their reproducible particle/cluster sizes. More importantly, such a positive surface charge is a strong indicator of the presence of partially hydrolyzed surface structures, such as $\equiv U(OH)^+$ on the crystalline primary particles; i.e., the intermediate structures between $UO_2(cr)$ and $U(OH)_n^{4-n}(aq)$. The occurrence of such intermediate structure formation has been proposed in previous studies on iron oxide nanoparticle formation [37].

The size and zeta-potential values of the $U(IV)_{NPs}$ were measured for a wide range of pHs to identify their colloidal properties under various reaction conditions of the NPP hydrolysis. Without pH adjustment, the pH of the 1 mM sample, which was prepared from a $U(IV)_{NPs}$ stock solution, was approximately 2.3, as shown in Figure 1c,d. By the addition of 0.1 M NaOH, the size of $U(IV)_{NPs}$ clusters increases with the solution pH, as shown in Figure S3. At a relatively high pH, it appears that the $U(IV)_{NPs}$ clusters start aggregating by forming relatively large clusters up to the micrometer scale. In fact, the zeta-potential values decrease slightly but remain at positive up to pH 8. However, the zeta-potential values of the $U(IV)_{NPs}$ became negative (< -20 mV) at pH 9. The isoelectric point was found to be located approximately at pH 8.6, although precise pH control was difficult at that pH region. Thus, it was expected that the sizes of the $U(IV)_{NPs}$ were maintained at approximately in the range of 250–650 nm during the NPP hydrolysis that was examined in this study.

3.2. Comparison of NPP Hydrolysis Rates by Different $U(IV)$ Species

The hydrolysis of NPP was investigated with two different types of $U(IV)$ species, including $U(IV)_{NPs}$ and amorphous $U(IV)$ -hydroxides ($U(IV)-OH(am)$). The detailed preparation procedures for each species are provided in the Materials and Methods Section. The strong absorptivities of NPP and NP were exploited to monitor the reaction kinetics by UV-Vis spectroscopy, as shown in Figure 2. The spectra were within the range of 210–500 nm, where the characteristic λ_{max} values of NPP (plus NPPH and the reaction intermediates) and NP appeared at 290–310 nm (a and b_1 in Figure 2) and at 400 nm (b_2), respectively.

Interestingly, our reaction kinetic monitoring system shows that the NPP hydrolysis with $U(IV)_{NPs}$ occurred via a multi-step reaction pathway involving a very rapid NPP- $U(IV)_{NPs}$ complexation. As shown in Figure 2, a series of transient spectra (dashed lines) indicated by an arrow (a) appeared immediately after the injection of $U(IV)_{NPs}$ into the NPP solution at pH 7.5. These spectra are distinct from that of NPP (a dianionic form, pK_a 5.1), and the initial spectrum of the series (" a " in Figure 2) exhibits a band shape similar to that of NPPH. Therefore, we attribute the initial spectrum to the first intermediate ($I1$). The formation of $I1$ was immediate and far faster than the following steps, and thus could not be measured in our typical data collecting interval (2 s). Thus, the band shift shown in series (a) during the initial 30 s (dashed lines in Figure 2) was interpreted as a subsequent transformation of $I1$ to another more stable intermediate ($I2$). The absorption spectra of the reaction mixture collected at 25 °C (see Figure S4a) also demonstrates that the band shift pattern is similar to that recorded at 50 °C (see Figure 2) except regarding the reaction rate. The initial process (a) (dashed lines) takes about 200 s at 25 °C reaction and 30 s at 50 °C reaction. Thus, it is concluded that both reactions at 25 and 50 °C follow the same reaction pathway accompanying the initial changes (a) in Figure 2. However, such transient spectra were not observed in the spectra obtained from the NPP hydrolysis with $U(IV)-OH(am)$ (see Figure S4b). More details about $I1$ and $I2$ are included in Section 3.3 below, which describes the mechanistic studies on the hydrolysis of NPP.

The absorption spectra of NPP and NP at various concentrations and pH ranges are represented in Figure S5 and were applied to convert the absorbance values to the concentration of each species. Pseudo-first order rate constants (k_{obs}) were calculated from the absorbance increase at 400 nm (λ_{max} of NP, $\epsilon = 18,500 \text{ cm}^{-1} \text{ M}^{-1}$) over a period sufficient for a 10% reaction conversion to be achieved

(normally up to 100 s, indicated as a dotted line in the inset plot of Figure 2). The rate constants obtained as the mean values from triplicate runs with $\pm 10\%$ reproducibility are summarized in Table 1 (The equations for calculating the rate constants are provided in Supplementary Materials).

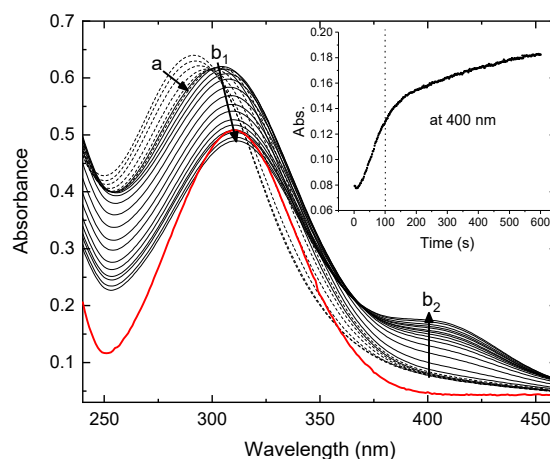
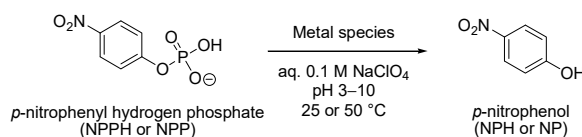


Figure 2. Absorption spectra of the free NPP (thick red) and reaction mixture (black) collected for initial 600 s ($[NPP] = 50 \mu\text{M}$, $[U(IV)_{NPs}] = 100 \mu\text{M}$ in 0.1 M NaClO_4 , pH = 7.5, 50 °C); dashed lines (arrow a): initial transition between two intermediates adsorbed on the surfaces of $U(IV)_{NPs}$; solid black lines: reduction of intermediate 2 (arrow b_1); and formation of reaction product NP: arrow b_2 .

To identify the active species actually responsible for the rapid hydrolysis by $U(IV)_{NPs}$, the reactivities of the $U(IV)\text{-OH(am)}$ were compared. For $U(IV)\text{-OH(am)}$, the formation of $UO_2 \cdot xH_2O(am)$ was prevalent over a wide pH range. At low pH (<5), hydrolyzed $U(IV)$ species such as oligomeric $U(IV)\text{-OH}$ species may exist. Hypothetically, $U(IV)_{NPs}$ may not be the reactive species and may slowly transform into a more thermodynamically stable and more reactive $U(IV)$ species for phosphoester hydrolysis after addition into a given test solution. However, $U(IV)\text{-OH(am)}$ and other $U(IV)$ species were found to be less reactive than the $U(IV)_{NPs}$, as shown in Table 1. Thus, we concluded that the high reaction rates of $U(IV)_{NPs}$ originated from their intrinsic physicochemical properties, such as particle size, surface charge, and chemical structure.

Table 1. Comparison of the kinetic data of $U(IV)$ and other metal ions for inducing NPP hydrolysis.



Metal Species	T (°C)	$k_{\text{obs}}/10^{-4} \text{ s}^{-1}$					
		pH 3.3 ± 0.2	pH 5.2 ± 0.2	pH 6.1 ± 0.2	pH 7.2 ± 0.3	pH 9.3 ± 0.2	
$U(IV)_{NPs}$	25	0.90	1.1	1.2	1.4	0.21	this work [a]
	50	15	16	19	20	2.2	
$U(IV)\text{-OH(am)}$	25	0.24	0.23	0.21	0.17	0.080	
	50	2.4	2.3	2.2	1.7	0.82	
$U(VI)$, $Th(IV)$, $La(III)$	37		0.095(UO_2^{2+}) [b]	280(Th^{4+}) [c]	0.0014(La^{3+}) [d]		ref. [37–39] [f]
$Ce(IV)$ [e]	50			180	260	190	ref. [40,41] [f]

[a] pH: the average values of each reaction; conditions: $[substrate] = 50 \mu\text{M}$, $[U(IV)] = 100 \mu\text{M}$ in 0.1M NaClO_4 . Kinetic data were collected at 400 nm; for [b], [c], [d], and [e], 10-fold, 20-fold, 2.5-fold (at 25 °C), and 40-fold excesses of metal over substrate were used, respectively; [f] bis(4-nitrophenyl) phosphate was used as the substrate of the hydrolysis.

The level of the hydrolysis rate enhancement of $U(IV)_{NPs}$ is comparable (i.e., about an order lower) to that of $Ce(IV)$ and is also ca. 200 and 10^3 times higher than those of the UO_2^{2+} and La^{3+} catalyzed cleavages, respectively (see Table 1). We employed a 2-fold excess of $U(IV)$ over the substrates, which is a much smaller amount compared to those reported previously (2.5–40-fold excess) [38–42] because the high concentration of metal can induce significant precipitation of metal at a high pH range. To compare the reactivities of other metals, the $U(IV)$ concentration in a solution is expressed in molar units. Thus, it represents the total U content added into the reaction solution, not that of active or/and dissolved U species only.

The reactions with $U(IV)_{NPs}$ exhibited a characteristic pH dependency, i.e., a gradual increase up to pH 7, followed by a drastic decrease at a pH higher than 7 (see Table 1). Such a reduction in the reactivity indicates that the bulk hydroxide ions in an aqueous phase do not act as a nucleophile to attack the phosphorus center. Instead, the NPP hydrolysis at pH 7 and lower is facilitated by the surface-bound hydroxides on the nanoparticles. The sharp decrease in the rate at pH >7 can be explained well by the colloidal destabilization, including particle aggregation and the surface potential changes from positive to negative values (see Figure S3). Thus, the adsorption of the NPP can be dependent on pH and affect the reaction rate; at higher pH the surface of $U(IV)_{NPs}$ is no more effective to attract ligands and catalyze NPP hydrolysis. Conversely, the low-pH reaction rate is slightly higher than those obtained from high pH solutions for $U(IV)-OH(am)$. Even for this modest increase in reactivity, we speculate that the $U(IV)_{NPs}$ formed from hydrolyzed $U(IV)$ species probably play a role, because $U(IV)_{NPs}$ clusters or primary particles can be gradually produced over time under mild acidic conditions.

Further spectrophotometric analysis was conducted by varying the NPP and $U(IV)_{NPs}$ concentrations. As shown in Figure S6, the initial rate depends on the NPP concentration. By increasing the NPP concentration from 25 μM to 100 μM , the rate constant (k_{obs}) increases from $7.5 \times 10^{-3} s^{-1}$ up to $3.1 \times 10^{-2} s^{-1}$, which is ca. 10^6 times greater than that of the reaction without any metal complexes ($k_{obs} = 3.3 \times 10^{-8} s^{-1}$) [43]. At a fixed substrate concentration (50 μM NPP), the reaction rate was also found to be proportional to the $U(IV)_{NPs}$ concentration; the rate constant of $1.1 \times 10^{-2} s^{-1}$ in Figure S6 with 500 μM $U(IV)_{NPs}$ is almost five times greater than that from Table 1 for 100 μM $U(IV)_{NPs}$. In addition, it should be noted that after the rapid initial stage, the reaction slows down, as shown in the inset of Figure 2 (>100 s). Such a decrease in the reaction rate is largely due to the reduction in the substrate concentration. However, we suppose that the surface poisoning effect is also involved in $U(IV)_{NPs}$ via the phosphate ion that remained bound after the release of NP.

3.3. Mechanistic Studies on the NPP Hydrolysis

3.3.1. ATR-FTIR Studies and SEIRA

Here, surface-enhanced infrared absorption (SEIRA) was employed for the first time to study the reaction mechanism of NPP hydrolysis on the surfaces of $U(IV)_{NPs}$. SEIRA is a near-field phenomenon, in which the IR absorption of molecules adsorbed on or in the vicinity of small metal/metal oxide-clusters is enhanced by a factor of 10 to 1000 due to the electrical field around the clusters [44]. The surface selection rule of SEIRA implies that only the vibrational modes inducing dynamic dipole moments perpendicular to the surface will be enhanced, which can provide the structural information regarding the bound molecules and their orientation [45]. Usually, *p*-nitrobenzoic acid or its derivatives are used as model substrates. In this study, we report that $U(IV)_{NPs}$ induce SEIRA for NPP. As demonstrated in Figure 3a, the overall IR absorption of 5 mM NPP is enhanced in the presence of 1 mM $U(IV)_{NPs}$. The strong band at 1350 cm^{-1} has been assigned as a symmetric NO_2 stretching vibrational mode in previous SEIRA studies and is used to examine the molecular orientation of the ligand adsorbed on noble metal-based and metal oxide-based nanoparticle systems [46,47]. For the enhanced IR spectrum in Figure 3a, both surface bound and unbound NPP molecules contribute to the IR absorption, while free (unbound) NPP remains dominant.

Figure 3b shows the SEIRA effect more clearly. Without $U(IV)_{NPs}$ the band at 1350 cm^{-1} is overly weak in a solution of 0.1 mM NPP, and cannot be detected in a given ATR-FTIR setting (dashed line, and see Figure S7a for the full spectrum); however, the addition of 0.1 mM $U(IV)_{NPs}$ significantly enhances the intensities of the peaks. The enhancement factor is ca. 100 in the presence of 1 mM of $U(IV)_{NPs}$; however, no further increase is obtained by adding more than 1.5 mM $U(IV)_{NPs}$, probably due to the full adsorption of phosphoesters onto the nanoparticle surfaces [48]. To further evaluate the SEIRA of NPP, the NPP concentration was varied at a fixed concentration of $U(IV)_{NPs}$ (1 mM , see Figure S8). The SEIRA was only observed up to a certain level of NPP concentration (ca. 1 mM), where the surface saturation of $U(IV)_{NPs}$ with NPP was attained. Overall, such SEIRA effects indicate that the crystalline primary particles of $U(IV)_{NPs}$ possessing UO_2 -like semiconductor properties can effectively create polarized local electromagnetic fields interacting with the oscillating dipoles of the adsorbed molecules [46,47].

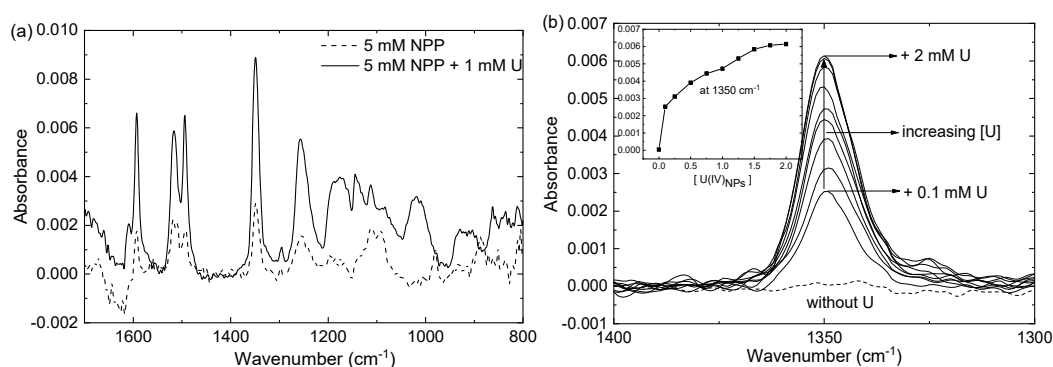


Figure 3. ATR-FTIR spectra of the reaction mixture exhibiting SEIRA effects at pH 5.2. (a) New peaks are observed in the spectrum of NPP in the presence of $U(IV)_{NPs}$ (solid) compared to the case with the free NPP (dashed). (b) Expanded spectra at $1300\text{--}1400\text{ cm}^{-1}$ (dashed line: 0.1 mM NPP without $U(IV)_{NPs}$; solid lines: upon addition of $0.1\text{--}2\text{ mM}$ $U(IV)_{NPs}$ to 0.1 mM NPP (pH 3.2–2.0)).

The SEIRA spectrum of NPP bound to $U(IV)_{NPs}$ (Figure S7b) was further examined to elucidate its spectral difference from that of the free NPP in the low frequency region, where the vibrational modes of the phosphate groups were dominant. The SEIRA spectrum of NPP- $U(IV)_{NPs}$ (red line in Figure S7b) exhibits two discrete vibrational bands compared with that of the free NPP (black line in Figure S7b) at ~ 1150 and $\sim 1025\text{ cm}^{-1}$. In this spectrum, the characteristic P-O and P-OH bands of the free phosphates occurring at approximately 1200 , 1080 , and 980 cm^{-1} are absent. In previous studies for a phosphomonoester-ferrihydrite or -goethite system, the authors assigned the bands near 1150 cm^{-1} and 1030 cm^{-1} to the P-O vibrations, which indicated the significant distortions of the P-O bonds as phosphomonoesters coordinated to goethite [25,49,50]. Additionally, in their structural interpretation of phosphate/phosphonate surface complexes, either a bidentate coordination or a monodentate coordination in combination with hydrogen bonding to neighboring surface oxometallic sites was favored [25,49–51]. Thus, in the NPP- $U(IV)_{NPs}$ system, we speculate that inner-sphere surface complexes are formed on $U(IV)_{NPs}$, and more specifically, two terminal oxygens of the phosphate are fully coordinated to the particle surfaces; i.e., in a bidentate fashion. This arrangement may contribute to the SEIRA effect of the NPP- $U(IV)_{NPs}$ system by preferentially enhancing vibrational modes that have dipole moment derivative components perpendicular to the surface [48]. In this study, this surface complex was considered to be one of the reaction intermediates, particularly one that was accumulated at the rate-determining step.

3.3.2. ATR-FTIR Spectra of Solid Phase $U(IV)_{NPs}$

ATR-FTIR spectroscopic analyses were performed to further investigate the surface adsorption of phosphoester/phosphate on the surfaces of $U(IV)_{NPs}$. To identify the surface complex of the final

reaction product, two parallel samples, one with NPP and the other with phosphate, were prepared at pH 7. Under our experimental conditions, an excess amount (10 equiv) of $U(IV)_{NPs}$ was used to complete the reaction (100% conversion of NPP to NP) and the precipitate was formed after the hydrolysis of NPP. Figure 4 shows the spectra of the dried precipitates from each reaction. The positions of peaks (1100, 1030, 920, and 860 cm^{-1}) from the NPP reaction precipitate (solid line in Figure 4) are almost identical to the phosphate reaction precipitate (dashed line in Figure 4), which shifted from the peaks of the phosphate solution (pH 7) without $U(IV)_{NPs}$. In previous studies, Arai and Sparks also observed similar peak positions in the spectra of phosphate adsorbed on goethite surfaces [51]. We, therefore, conclude that the model phosphoester, NPP, was finally decomposed to the phosphate surface complex on the $U(IV)$ precipitates at pH 7 by the hydrolysis.

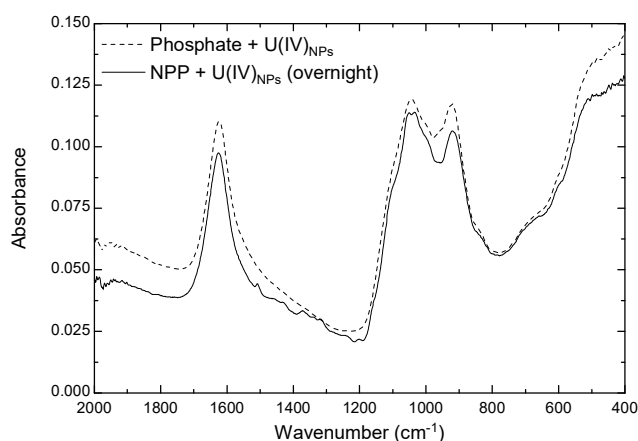
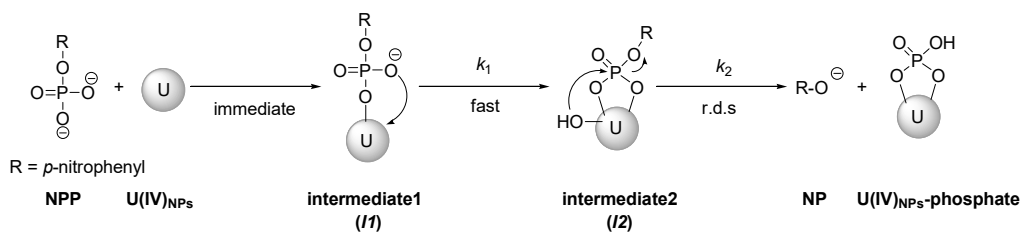


Figure 4. ATR-FTIR spectra of the dried precipitates from each of the two reactions: one with phosphate and the other with NPP. $[U(IV)_{NPs}] = 1.5$ mM, $[Substrate] = 0.15$ mM, $I = 0.1$ M $NaClO_4$ at pH 7, 25 °C, overnight.

Based on our findings, a multi-step reaction mechanism for the hydrolysis of NPP was postulated, as illustrated in Scheme 1. In this mechanism, the reaction starts with the immediate adsorption of NPP on the surface of the $U(IV)_{NPs}$ to form a surface complex, *I1*, as an outer-sphere $U(IV)_{NPs}$ -NPP complex. Subsequently, *I1* rapidly changes its structure to the more stable complex (*I2*) that exhibits SEIRA. An intramolecular attack on *I2* by the surface-bound hydroxide available on $U(IV)_{NPs}$ is the rate-determining step (r.d.s.) for the release of the products, *p*-nitrophenolates (NP). For the slow kinetics at pH 9 as shown in Table 1 we think that the surface turns negative and exhibit more amorphous $U(IV)$ -OH-like properties; i.e., oxyhydroxy structures on $U(IV)_{NPs}$ surfaces. Thus, the rate of r.d.s. could become slower due to the less available surface-bound hydroxides ($-U-OH$).

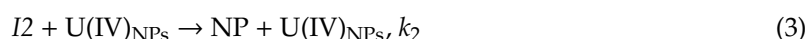
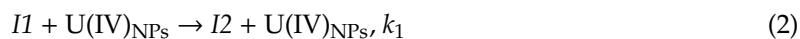


Scheme 1. Proposed mechanism for the hydrolysis of NPP.

3.3.3. Reaction Modeling Analysis

Finally, a chemical modeling study was carried out to confirm the reaction mechanism, and the rate constants are listed in Table 1. The kinetic spectrophotometric data were analyzed using the ReactLab™ KINETICS program (see Figures S9–S11). A series of full spectra, as shown in Figure 2, and the reaction

model (Equations (2) and (3)), as described below, were subjected to numerical analysis for fitting the global reaction parameters [52,53]. All species, including $U(IV)_{NPs}$ that exhibited absorption within the 200–500 nm wavelength range, were included in the model. However, for the first reaction (Equation (1)), producing $I1$ was excluded from the model because it was overly fast, and thus could not be monitored in this study. The pK_a of the NP was also provided to the reaction model as an auxiliary parameter (Equation (4)).



Overall, such a reaction model analysis was successful for pH values between 6 and 9, where the emergence of the spectral band (~400 nm) of the NP (the reaction product) was evident. At pH 7, the pseudo-first order rate constants we calculated were $5.7 \times 10^{-2} \text{ s}^{-1}$ for k_1 and $1.4 \times 10^{-3} \text{ s}^{-1}$ for k_2 ; note that k_2 is close to k_{obs} ($2.0 \times 10^{-3} \text{ s}^{-1}$) at pH 7 in Table 1. The rate constants of the k_1 level were found to be 10 to 100 times higher than those of the k_2 level and were pH-dependent (see Figures S9–S11). The pH dependency of k_1 likely indicates the acidic property of Intermediate 1 ($I1$) as that of NPP itself. Thus, we expect that the higher the pH, the more the base (or deprotonated) form of $I1$, which may be more prone to facilitate the transformation of $I1$ to $I2$ (i.e., to induce the higher k_1). All the results calculated from the reaction modeling are demonstrated as a function of pH in Figure 5. Generally, the k_2 values for the rate-determining step match the k_{obs} values in Table 1 within the same order of magnitude. In addition, an excellent fit between the simulated and experimental spectra was obtained at various pH levels (Figures S9–S11). Thus, we confirm that the model used in this study is appropriate for representing the mediated hydrolysis reaction of $U(IV)_{NPs}$.

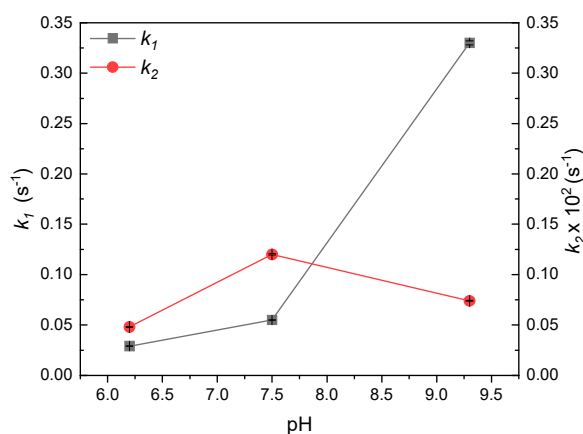


Figure 5. Influence of pH on the pseudo-first order rate constants, k_1 (black squares) and k_2 (red circles), calculated by ReactLab KINETICS program for the NPP hydrolysis mediated by $U(IV)_{NPs}$ at 50 °C for 100 s.

3.4. Implication of $U(IV)_{NPs}$ Reactivity

Understanding the speciation, mechanism, and kinetics of U transformation under various conditions relevant to natural and engineered systems is essential to predicting and controlling the migration of U in contaminated environments. Recently, bioreduction accompanied by the phosphate-precipitated $U(VI)$ phase has been considered as a potential pathway for U transformation to $U(IV)$ -phosphate mineral phases that could further limit U mobility [12,14]. Previous studies have shown that such processes can compete with or limit uraninite formation during the bioreduction of aqueous $U(VI)$ in the presence of dissolved phosphates [54]. In this study, we demonstrated

that nanocrystalline $U(IV)_{NPs}$ possess their own chemical reactivity toward both inorganic and organic phosphates. Positive surface charges of $U(IV)_{NPs}$ formed at acidic to circumneutral pH levels can strongly drive the surface complexation with anionic ligands, as attested by the measured zeta-potential values of $U(IV)_{NP}$ -colloids in aqueous solutions and the rapid initial reaction kinetics shown in Scheme 1. Multivalent anions, e.g., phosphates, are very likely to form stable surface complexes on $U(IV)_{NPs}$, simultaneously inducing the reduction of their colloidal stability and $U(IV)$ precipitation. However, the concentration of free orthophosphate is often low in groundwater, and most of the available phosphorus is in the form of organic compounds [55]. Our mechanistic study suggests that organophosphates of microbial metabolic origin, or as supplements of amended treatment in contaminated sites, can rapidly produce phosphate- $U(IV)_{NPs}$ complexes that subsequently transform into uranium phosphate precipitates, of which the rate should depend on the U-to-phosphates ratio and pH in aqueous environments.

4. Conclusions

In summary, the synthetic $U(IV)_{NPs}$ were shown to be reactive species that can enhance the hydrolysis of NPP, among the other forms of the $U(IV)$ species, at pH 3–10. The positive surface charges and the high surface areas originating from the rough cluster morphology composed of primary particles could be the major factors facilitating the surface adsorption of NPP anions on the $U(IV)_{NPs}$ for the hydrolysis. The reaction kinetics and mechanism of the phosphoester cleavage mediated by $U(IV)_{NPs}$ were explored in detail. A multi-step reaction mechanism proposed in this study involving two surface complex intermediates, i.e., *I1* and *I2*, was supported by various spectroscopic data analysis results. Based on our ATR-FTIR studies, we suggest that the inner-sphere surface complexes responsible for inducing the SEIRA of NPP bound to $U(IV)_{NPs}$ are involved in the rate-determining step of the NPP hydrolysis. Finally, this study indicates that $U(IV)_{NPs}$, owing to the unique nanocolloidal properties, could be one of the major $U(IV)$ species that actively participates in the phosphate-bound $U(IV)$ mineral formation via interacting with organophosphates in reduced environments. The strategy for U immobilization developed in this study is applicable to transforming colloidal U particles to U-phosphate precipitates and to delaying their potential migration in contaminated sites using organophosphates. Thus, our results will aid understanding chemical behaviors of U species, especially, colloidal U particles interacting with aqueous phase components in sediments and soils.

Supplementary Materials: The Supplementary Materials are available online: <http://www.mdpi.com/2504-5377/3/4/63/s1>.

Author Contributions: Conceptualization, methodology, software, and validation, H.C. and W.C.; formal analysis, investigation, resources, data curation, and writing—Original draft preparation, H.C.; writing—Review and editing, W.C.; visualization, H.C.; supervision, W.C.; project administration, W.C.; funding acquisition, W.C.

Funding: This research was funded by the Nuclear Research and Development program of the National Research Foundation of Korea, grant number 2017M2A8A5014719.

Conflicts of Interest: The authors declare no conflict of interest. The funders had no role in the design of the study; in the collection, analyses, or interpretation of data; in the writing of the manuscript, or in the decision to publish the results.

References

1. Kim, J.-I. Significance of actinide chemistry for the long-term safety of waste disposal. *Nucl. Eng. Technol.* **2006**, *38*, 459–482.
2. Opel, K.; Weiss, S.; Hübener, S.; Zänker, H.; Bernhard, G. Study of the solubility of amorphous and crystalline uranium dioxide by combined spectroscopic methods. *Radiochim. Acta* **2007**, *95*, 143–149. [[CrossRef](#)]
3. Kim, J.I. Actinide colloid generation in groundwater. *Radiochim. Acta* **1991**, *52*, 71–82. [[CrossRef](#)]
4. Maher, K.; Bargar, J.R.; Brown, G.E., Jr. Environmental speciation of actinides. *Inorg. Chem.* **2012**, *52*, 3510–3532. [[CrossRef](#)] [[PubMed](#)]

5. Geckeis, H.; Rabung, T.; Schäfer, T. Actinide-nanoparticle interaction: Generation, stability and mobility. In *Actinide Nanoparticle Research*; Springer: Berlin/Heidelberg, Germany, 2011; pp. 1–30. [[CrossRef](#)]
6. Fuller, C.; Bargar, J.; Davis, J.; Piana, M. Mechanisms of uranium interactions with hydroxyapatite: Implications for groundwater remediation. *Environ. Sci. Technol.* **2002**, *36*, 158–165. [[CrossRef](#)] [[PubMed](#)]
7. Murray, F.; Brown, J.; Fyfe, W.; Kronberg, B. Immobilization of U-Th-Ra in mine wastes by phosphate mineralization. *Can. Mineral.* **1983**, *21*, 607–610.
8. Arey, J.S.; Seaman, J.C.; Bertsch, P.M. Immobilization of uranium in contaminated sediments by hydroxyapatite addition. *Environ. Sci. Technol.* **1998**, *33*, 337–342. [[CrossRef](#)]
9. Jerden, J.L., Jr.; Sinha, A. Phosphate based immobilization of uranium in an oxidizing bedrock aquifer. *Appl. Geochem.* **2003**, *18*, 823–843. [[CrossRef](#)]
10. Langmuir, D. *Aqueous Environmental Geochemistry*; Prentice Hall: Upper Saddle River, NJ, USA, 1997.
11. Martinez, R.J.; Wu, C.H.; Beazley, M.J.; Andersen, G.L.; Conrad, M.E.; Hazen, T.C.; Taillefert, M.; Sobczyk, P.A. Microbial community responses to organophosphate substrate additions in contaminated subsurface sediments. *PLoS ONE* **2014**, *9*, e100383. [[CrossRef](#)]
12. Newsome, L.; Morris, K.; Trivedi, D.; Bewsher, A.; Lloyd, J.R. Biostimulation by glycerol phosphate to precipitate recalcitrant uranium (IV) phosphate. *Environ. Sci. Technol.* **2015**, *49*, 11070–11078. [[CrossRef](#)]
13. Newsome, L.; Morris, K.; Lloyd, J.R. The biogeochemistry and bioremediation of uranium and other priority radionuclides. *Chem. Geol.* **2014**, *363*, 164–184. [[CrossRef](#)]
14. Stetten, L.; Blanchart, P.; Mangeret, A.; Lefebvre, P.; Le Pape, P.; Brest, J.; Merrot, P.; Julien, A.; Proux, O.; Webb, S.M. Redox fluctuations and organic complexation govern uranium redistribution from U (IV)-phosphate minerals in a mining-polluted wetland soil, Brittany, France. *Environ. Sci. Technol.* **2018**, *52*, 13099–13109. [[CrossRef](#)] [[PubMed](#)]
15. Morin, G.; Mangeret, A.; Othmane, G.; Stetten, L.; Seder-Colomina, M.; Brest, J.; Ona-Nguema, G.; Bassot, S.; Courbet, C.; Guillevic, J. Mononuclear U (IV) complexes and ningyoite as major uranium species in lake sediments. *Geochem. Perspect. Lett.* **2016**, *2*, 95–105. [[CrossRef](#)]
16. Ingall, E.D.; Schroeder, P.A.; Berner, R.A. The nature of organic phosphorus in marine sediments: New insights from ³¹P NMR. *Geochim. Cosmochim. Acta* **1990**, *54*, 2617–2620. [[CrossRef](#)]
17. Espinosa, M.; Turner, B.L.; Haygarth, P.M. Preconcentration and separation of trace phosphorus compounds in soil leachate. *J. Environ. Qual.* **1999**, *28*, 1497–1504. [[CrossRef](#)]
18. Pant, H.; Warman, P.; Nowak, J. Identification of soil organic phosphorus by ³¹P nuclear magnetic resonance spectroscopy. *Commun. Soil Sci. Plant Anal.* **1999**, *30*, 757–772. [[CrossRef](#)]
19. Benitez-Nelson, C.R. The biogeochemical cycling of phosphorus in marine systems. *Earth-Science Reviews* **2000**, *51*, 109–135. [[CrossRef](#)]
20. Turner, B.L.; McKelvie, I.D.; Haygarth, P.M. Characterisation of water-extractable soil organic phosphorus by phosphatase hydrolysis. *Soil Biol. Biochem.* **2002**, *34*, 27–35. [[CrossRef](#)]
21. Paytan, A.; McLaughlin, K. The oceanic phosphorus cycle. *Chem. Rev.* **2007**, *107*, 563–576. [[CrossRef](#)]
22. Balistrieri, L.S.; Chao, T. Adsorption of selenium by amorphous iron oxyhydroxide and manganese dioxide. *Geochim. Cosmochim. Acta* **1990**, *54*, 739–751. [[CrossRef](#)]
23. Baldwin, D.S.; Beattie, J.K.; Coleman, L.M.; Jones, D.R. Phosphate ester hydrolysis facilitated by mineral phases. *Environ. Sci. Technol.* **1995**, *29*, 1706–1709. [[CrossRef](#)] [[PubMed](#)]
24. Baldwin, D.S.; Beattie, J.K.; Coleman, L.M.; Jones, D.R. Hydrolysis of an organophosphate ester by manganese dioxide. *Environ. Sci. Technol.* **2001**, *35*, 713–716. [[CrossRef](#)] [[PubMed](#)]
25. Olsson, R.; Giesler, R.; Loring, J.S.; Persson, P. Adsorption, desorption, and surface-promoted hydrolysis of glucose-1-phosphate in aqueous goethite (α -FeOOH) suspensions. *Langmuir* **2010**, *26*, 18760–18770. [[CrossRef](#)] [[PubMed](#)]
26. Morales-Rojas, H.; Moss, R.A. Phosphorolytic reactivity of o-iodosylcarboxylates and related nucleophiles. *Chem. Rev.* **2002**, *102*, 2497–2522. [[CrossRef](#)] [[PubMed](#)]
27. Sigel, H. Metal Ions in Biological Systems. In *The Lanthanides and Their Interrelations with Biosystems*; Sigel, H., Sigel, A., Eds.; CRC Press: Basel, Switzerland, 2003; Volume 40, pp. 369–440.
28. Liu, C.; Wang, M.; Zhang, T.; Sun, H. DNA hydrolysis promoted by di- and multi-nuclear metal complexes. *Coord. Chem. Rev.* **2004**, *248*, 147–168. [[CrossRef](#)]
29. Morrow, J.R.; Iranzo, O. Synthetic metallonucleases for RNA cleavage. *Curr. Opin. Chem. Biol.* **2004**, *8*, 192–200. [[CrossRef](#)]

30. Williams, N.H. Models for biological phosphoryl transfer. *Biochim. Biophys. Acta* **2004**, *1697*, 279–287. [[CrossRef](#)]
31. Yatsimirsky, A.K. Metal ion catalysis in acyl and phosphoryl transfer: Transition states as ligands. *Coord. Chem. Rev.* **2005**, *249*, 1997–2011. [[CrossRef](#)]
32. Ott, R.; Krämer, R. Rapid Phosphodiester Hydrolysis by Zirconium(IV). *Angew. Chem. Int. Ed.* **1998**, *37*, 1957–1960. [[CrossRef](#)]
33. Blaskó, A.; Bruice, T.C. Recent Studies of Nucleophilic, General-Acid, and Metal Ion Catalysis of Phosphate Diester Hydrolysis. *Acc. Chem. Res.* **1999**, *32*, 475–484. [[CrossRef](#)]
34. Lim, S.; Franklin, S.J. Lanthanide-binding peptides and the enzymes that Might Have Been. *Cell. Mol. Life Sci.* **2004**, *61*, 2184–2188. [[CrossRef](#)] [[PubMed](#)]
35. Luong, T.K.N.; Shestakova, P.; Parac-Vogt, T.N. Kinetic studies of phosphoester hydrolysis promoted by a dimeric tetrazirconium(IV) Wells–Dawson polyoxometalate. *Dalton Trans.* **2016**, *45*, 12174–12180. [[CrossRef](#)] [[PubMed](#)]
36. Cohen, D.; Carnall, W.T. Absorption spectra of Uranium(III) and Uranium(IV) in DCIO₄ solution 1. *J. Phys. Chem.* **1960**, *64*, 1933–1936. [[CrossRef](#)]
37. Jolivet, J.P.; Tronc, E.; Chanéac, C. Iron oxides: From molecular clusters to solid. A nice example of chemical versatility. *Geomaterials (Mineralogy)* **2006**, *338*, 488–497. [[CrossRef](#)]
38. Takasaki, B.K.; Chin, J. Synergistic effect between lanthanum (III) and hydrogen peroxide in phosphate diester cleavage. *J. Am. Chem. Soc.* **1993**, *115*, 9337–9338. [[CrossRef](#)]
39. Moss, R.A.; Bracken, K.; Zhang, J. Actinide (uranyl) hydrolysis of phosphodiester. *Chem. Commun.* **1997**, 563–564. [[CrossRef](#)]
40. Moss, R.A.; Zhang, J.; Bracken, K. Extraordinary acceleration of phosphodiester hydrolyses by thorium cations. *Chem. Commun.* **1997**, 1639–1640. [[CrossRef](#)]
41. Schneider, H.J.; Rammo, J.; Hettich, R. Catalysis of the hydrolysis of phosphoric acid diesters by lanthanide ions and the influence of ligands. *Angew. Chem. Int. Ed.* **1993**, *32*, 1716–1719. [[CrossRef](#)]
42. Bracken, K.; Moss, R.A.; Ragunathan, K.G. Remarkably rapid cleavage of a model phosphodiester by complexed ceric ions in aqueous micellar solutions. *J. Am. Chem. Soc.* **1997**, *119*, 9323–9324. [[CrossRef](#)]
43. Breslow, R.; Huang, D.-L. Effects of metal ions, including Mg²⁺ and lanthanides, on the cleavage of ribonucleotides and RNA model compounds. *Proc. Natl. Acad. Sci. USA* **1991**, *88*, 4080–4083. [[CrossRef](#)]
44. Griffiths, P.R. Surface-enhanced infrared absorption spectroscopy: Principles and applications. *Spectrosc. Prop. Inorg. Organomet. Compd.* **2013**, *44*, 95–122. [[CrossRef](#)]
45. Osawa, M.; Ataka, K.-I.; Yoshii, K.; Nishikawa, Y. Surface-enhanced infrared spectroscopy: The origin of the absorption enhancement and band selection rule in the infrared spectra of molecules adsorbed on fine metal particles. *Appl. Spectrosc.* **1993**, *47*, 1497–1502. [[CrossRef](#)]
46. Osawa, M.; Ikeda, M. Surface-enhanced infrared absorption of p-nitrobenzoic acid deposited on silver island films: Contributions of electromagnetic and chemical mechanisms. *J. Phys. Chem.* **1991**, *95*, 9914–9919. [[CrossRef](#)]
47. Ahmad, I.; Dines, T.J.; Rochester, C.H.; Anderson, J.A. IR study of nitrotoluene adsorption on oxide surfaces. *J. Chem. Soc., Faraday Trans.* **1996**, *92*, 3225–3231. [[CrossRef](#)]
48. Osawa, M. Surface-enhanced infrared absorption spectroscopy. In *Handbook of Vibrational Spectroscopy*; Chalmers, J., Griffiths, P., Eds.; John Wiley & Sons, Ltd.: Hoboken, NJ, USA, 2006; pp. 785–799. [[CrossRef](#)]
49. Li, B.; Raff, J.; Barkleit, A.; Bernhard, G.; Foerstendorf, H. Complexation of U (VI) with highly phosphorylated protein, phosvitin: A vibrational spectroscopic approach. *J. Inorg. Biochem.* **2010**, *104*, 718–725. [[CrossRef](#)]
50. Klein, A.R.; Bone, S.E.; Bakker, E.; Chang, Z.; Aristilde, L. Abiotic phosphorus recycling from adsorbed ribonucleotides on a ferrihydrite-type mineral: Probing solution and surface species. *J. Colloid Interface Sci.* **2019**, *547*, 171–182. [[CrossRef](#)]
51. Arai, Y.; Sparks, D.L. ATR–FTIR spectroscopic investigation on phosphate adsorption mechanisms at the ferrihydrite–water interface. *J. Colloid Interface Sci.* **2001**, *241*, 317–326. [[CrossRef](#)]
52. Maeder, M.; Neuhold, Y.-M. Practical data analysis in chemistry. In *Data Handling in Science and Technology*; Rutan, S., Walczak, B., Eds.; Elsevier: Oxford, UK, 2007.
53. Maeder, M.; King, P. *ReactLab KINETICS*; Jplus Consulting Pty Ltd.: East Freemantle, WA, Australia, 2009.

54. Salome, K.R.; Green, S.J.; Beazley, M.J.; Webb, S.M.; Kostka, J.E.; Taillefert, M. The role of anaerobic respiration in the immobilization of uranium through biomineralization of phosphate minerals. *Geochim. Cosmochim. Acta* **2013**, *106*, 344–363. [[CrossRef](#)]
55. Turner, B.L.; Papházy, M.J.; Haygarth, P.M.; McKelvie, I.D. Inositol phosphates in the environment. *Philos. Trans. R. Soc. Lond. Ser. B Biol. Sci.* **2002**, *357*, 449–469. [[CrossRef](#)]



© 2019 by the authors. Licensee MDPI, Basel, Switzerland. This article is an open access article distributed under the terms and conditions of the Creative Commons Attribution (CC BY) license (<http://creativecommons.org/licenses/by/4.0/>).